CHEMISTRY OF MATERIALS

pubs.acs.org/cm

Article

# Crystal Structure, Magnetism, and Electronic Properties of a Rare-Earth-Free Ferromagnet: $MnPt_5As$

Xin Gui and Weiwei Xie*

Cite This: *Chem. Mater.* 2020, 32, 3922−3929

Read Online

ACCESS | Metrics & More | Article Recommendations | Supporting Information

**ABSTRACT:** The design and synthesis of targeted functional materials have been long-term goals for materials scientists. Although a universal design strategy is difficult to generate for all types of materials, it is still helpful for individual families of materials to have such design rules. Herein, we incorporated several significant chemical and physical factors relevant to magnetism, such as structure-type, atomic distance, and spin−orbit coupling, and have thereby successfully synthesized a new rare-earth-free ferromagnet, $MnPt_5As$, for the first time. $MnPt_5As$ can be prepared by high-temperature pellet methods. According to the X-ray diffraction results, $MnPt_5As$ crystallizes in a tetragonal unit cell with the space group $P4/mmm$ (Pearson symbol $tP7$). Magnetic measurements on $MnPt_5As$ confirm ferromagnetism in this phase with a Curie temperature of ~301 K and a saturated moment of 3.5 $\mu_B$ per formula unit. Evaluation by applying the Stoner criterion also indicates that $MnPt_5As$ is susceptible to ferromagnetism. Electronic structure calculations using the WIEN2k program with local spin density approximation imply that the spontaneous magnetization of this phase arises primarily from the hybridization of the d orbitals on both Mn and Pt atoms. The theoretical assessments are consistent with the experimental results. Moreover, spin−orbit coupling effects heavily influence the magnetic moments in $MnPt_5As$. $MnPt_5As$ is the first ferromagnetic material in the $MgPt_5As$ structure-type. The discovery of $MnPt_5As$ offers a platform to study the interplay between magnetism and structure.

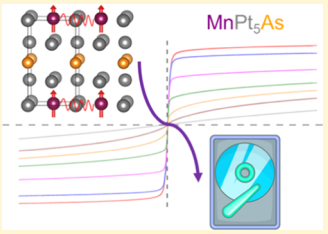




## INTRODUCTION

How one can easily approach new ferromagnetic materials (e.g., create a practical design strategy), especially to induce high transition temperatures and high saturated moments, is a demanding necessity for materials synthetic materials scientists. Meanwhile, the exploration of ferromagnetic intermetallic materials without strategically vulnerable rare-earth elements is critical for information technology applications, such as magnetic and magnetoelastic sensors,[1] hard-disk drives,[2] spintronics,[3−5] and biomedical devices.[6] Most research focuses on using magnetically active 3d transition metals such as Fe and Co to replace rare-earth elements.[7−10] Some of the 3d elements are ferromagnetically ordered above room temperature (e.g., Fe, Co, and Ni).[11] When alloyed with other elements, the magnetic and mechanic properties can be tuned accordingly.[12,13] AlNiCo-type magnetic systems, for example, have attracted attention for their temperature stability and mechanical properties. AlNiCo has a relatively large coercivity primarily due to the shape anisotropy of nanosized particles rather than the magnetocrystalline anisotropy that is typical for rare-earth-based magnets.[14−18] Later, quite a few Mn-based alloys were discovered to exhibit ferromagnetism, including Mn−B, Mn−Ga, Mn−Ge, Mn−Sb, and Mn−As.[19] Particularly, Mn−Al[20−26] and hexagonal NiAs-type Mn−Bi alloys[27−32] have potential due to their large magnetic crystalline anisotropy.

Mn−Mn distances significantly affect how magnetic moments are ordered in some systems, such as $RMn_2Ge_2$ and $RMn_6Ge_6$ (R = heavy-lanthanide elements or Y).[33−35] Moreover, the distribution patterns of Mn atoms in AMnX-based compounds (A = Li, Ni, Cu, or La; X = As or Sb) are similar and are also related to the saturated moment per Mn atom.[36] In such systems, ferromagnetic ordering and high saturated magnetic moments are usually preferred for longer Mn−Mn distances, while shorter Mn−Mn distances favor antiferromagnetic interactions. With this intriguing feature of Mn atom geometries, our candidate system is the tetragonal $MgPt_5As$-type structure, which can be considered as an antitype structure of one of the most well-known heavy fermion superconductors, $CeCoIn_5$.[37] Among all four atomic sites in the $MgPt_5As$-type structure, if a Mn atom can be placed onto the Mg site, the neighboring Mn−Mn distance can reach over 4 Å, due to the periodicity of the unit cells and the change of atomic radii, which is comparable to the ferromagnetic cases in ref 36. Furthermore, with the electronic configuration of $[Ar]3d^54s^2$, Mn is well known to provide high magnetic moments in intermetallics. The spin−orbit coupling (SOC) effect is another crucial factor when designing new magnetic materials due to its ability to interact with the spin polarization (magnetism) of the material.[38] For example, a strong SOC

Received: January 19, 2020
Revised: April 23, 2020
Published: April 24, 2020

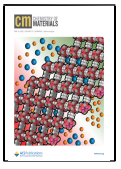







https://dx.doi.org/10.1021/acs.chemmater.0c00244
*Chem. Mater.* 2020, 32, 3922−3929

effect can enhance magnetocrystalline anisotropy, which is important for high coercivities and energy products in ferromagnets, such as FePt.[39,40] Heavy elements with 4d/5d or 5p/6p block electron orbital occupancy, platinum and bismuth, for example, are normally considered to be the source of strong SOC effects.

With these design rules in mind, we successfully designed and synthesized a new rare-earth-free ferromagnetic intermetallic compound $MnPt_5As$. Magnetic property measurements and theoretical calculations both show consistently that $MnPt_5As$ favors ferromagnetic ordering with a saturated moment of ~3.5 $\mu_B$ per formula. The magnetic moment in $MnPt_5As$ is theoretically proved to be strongly related to the atomic interaction between Mn and its neighboring Pt atoms. Meanwhile, $MnPt_5As$ is the first high-$T_c$ magnetic material in this structure-type. The discovery of $MnPt_5As$ paves a way to more remarkable magnetic compounds with similar structures.

## EXPERIMENTAL SECTION

**Preparation of Polycrystalline $MnPt_5As$.** Polycrystalline $MnPt_5As$ was synthesized by the high-temperature solid-state method. Mn powder, Pt powder, and As powder were evenly mixed and pelletized in an argon-filled glovebox due to the toxicity of arsenic.[41] The obtained pellet was placed in an alumina crucible and sealed into an evacuated silica tube (<$10^{-5}$ torr). The sample was heated up to 1050 °C at a rate of 30 °C/h and held for 2 days, followed by cooling to room temperature in 5 days. The polycrystalline product is air and moisture stable.

**Phase Identification.** The phase purity was determined by powder X-ray diffraction (PXRD) conducted on a Rigaku MiniFlex 600 powder X-ray diffractometer with Cu K$\alpha$ radiation ($\lambda$ = 1.5406 Å, Ge monochromator). The Bragg angle measured was from 5 to 90° at a rate of 0.1°/min with a step of 0.005°. Rietveld fitting in Fullprof was employed to obtain the weight percentage of the major phase $MnPt_5As$.[42]

**Structure Determination.** The crystal structure of $MnPt_5As$ was determined by single-crystal X-ray diffraction (SC-XRD). Multiple pieces of small crystals (~20 × 40 × 40 $\mu m^3$) were picked and measured by a Bruker Apex II diffractometer equipped with Mo radiation ($\lambda_{K\alpha}$ = 0.71073 Å) at room temperature. The small crystals were mounted on a Kapton loop with glycerol. Four different crystal orientations were chosen to take the measurements with an exposure time of 10 s per frame. The scanning 2$\theta$ width was set to 0.5°. Direct methods and full-matrix least-squares on $F^2$ within the ShelXtl package were applied to solve the structure.[43] Data acquisition was obtained via Bruker SMART software with the corrections of Lorentz and polarization effects done by the Saint program. Numerical absorption corrections were accomplished with XPrep.[44,45]

**Scanning Electron Microscope (SEM).** The crystal picture was taken using a high vacuum scanning electron microscope (SEM) (JSM-6610 LV). Samples were placed on carbon tape prior to loading into the SEM chamber and were examined at 20 kV.

**Physical Properties Measurements.** The Quantum Design Dynacool Physical Property Measurement System (PPMS) was used to measure the magnetic property and resistivity with the temperature range from 1.8 to 300 K with and without applied fields. The magnetic susceptibility is defined as $X = M/H$. Here, $M$ is the magnetization in units of emu and $H$ is the applied magnetic field. A standard relaxation calorimetry method was used to measure heat capacity and the data were collected in zero magnetic fields between 220 and 320 K using Apezon H-type grease. All of the measurements were performed on polycrystalline samples manually selected from $MnPt_5As$.

**Electronic Structure Calculations.** The electronic and ferromagnetic structures were calculated using the tight-binding, linear muffin-tin orbital-atomic sphere approximation (TB-LMTO-ASA) with the local (spin) density approximation (L(S)DA) method.[46−48] Empty spheres are required during the calculation, with the overlap of Wigner−Seitz (WS) spheres limited to smaller than 16%. A mesh of 9 × 9 × 6 $k$-points in the first Brillouin zone (BZ) was used to perform the detailed calculations and obtain the density of states (DOS) and crystal orbital Hamiltonian population (COHP) curves. The band structure, Fermi surfaces, and density of states (DOS) of $MnPt_5As$ were also calculated using the WIEN2k program, which has the full-potential linearized augmented plane wave method (FP-LAPW) with local orbitals implemented.[49,50] The electron exchange−correlation potential was used to treat the electron correlation within the generalized gradient approximation, which is parameterized by Perdew et. al.[51] The conjugate gradient algorithm was applied, and the energy cutoff was set at 500 eV. Reciprocal space integrations were completed over an 8 × 8 × 4 Monkhorst−Pack $k$-points mesh.[52] With these settings, the calculated total energy converged to less than 0.1 meV per atom. The spin−orbit coupling (SOC) effects were only applied for Pt atoms. The structural lattice parameters obtained from experiments were used for both calculations.

## RESULTS AND DISCUSSION

**Crystal Structure and Phase Determination of New-Phase $MnPt_5As$.** To obtain the structural feature of the new phase, a single crystal of $MnPt_5As$ was investigated. The refined results, crystallographic data, and anisotropic displacement parameters are shown in Table 1−3. $MnPt_5As$ crystallizes in a tetragonal structure with the space group $P4/mmm$ (No. 123). Mn located at 1c ($C_4$ symmetry), Pt atoms are on 1a ($C_4$ symmetry) and 4i ($C_2$ symmetry), and the As atom occupies 1b ($C_4$ symmetry) sites. Partial occupancy refinements were

**Table 1. Single-Crystal Structure Refinement for $MnPt_5As$ at 296(2) K**

| | |
|---|---|
| refined formula | $MnPt_5As$ |
| FW (g/mol) | 1105.31 |
| space group; $Z$ | $P4/mmm$; 1 |
| $a$ (Å) | 3.931(1) |
| $c$ (Å) | 7.092(1) |
| $V$ (Å$^3$) | 109.58(5) |
| $\theta$ range (deg) | 2.872−36.301 |
| no. reflections; $R_{int}$ | 1489; 0.0408 |
| no. independent reflections | 200 |
| no. parameters | 11 |
| $R_1$: $\omega R_2$ ($I > 2\delta(I)$) | 0.0275; 0.0730 |
| goodness of fit | 1.165 |
| diffraction peak and hole (e$^-$/ Å$^3$) | 4.430; −5.266 |

**Table 2. Atomic Coordinates and Equivalent Isotropic Displacement Parameters for $MnPt_5As$ at 296(2) K[a]**

| atom | Wyckoff | occ. | $x$ | $y$ | $z$ | $U_{eq}$ |
|---|---|---|---|---|---|---|
| Pt1 | 4i | 1 | 0 | 1/2 | 0.2794(1) | 0.0063(2) |
| Pt2 | 1a | 1 | 0 | 0 | 0 | 0.0058(2) |
| As3 | 1b | 1 | 0 | 0 | 1/2 | 0.0066(5) |
| Mn4 | 1c | 1 | 1/2 | 1/2 | 0 | 0.0073(8) |

[a]$U_{eq}$ is defined as one-third of the trace of the orthogonalized $U_{ij}$ tensor (Å$^2$).

**Table 3. Anisotropic Thermal Displacements from $MnPt_5As$**

| atom | U11 | U22 | U33 | U23 | U13 | U12 |
|---|---|---|---|---|---|---|
| Pt1 | 0.0064(2) | 0.0050(2) | 0.0075(3) | 0 | 0 | 0 |
| Pt2 | 0.0060(3) | 0.0060(3) | 0.0052(4) | 0 | 0 | 0 |
| As3 | 0.0069(7) | 0.0069(7) | 0.006(1) | 0 | 0 | 0 |
| Mn4 | 0.008(1) | 0.008(1) | 0.006(2) | 0 | 0 | 0 |


https://dx.doi.org/10.1021/acs.chemmater.0c00244
Chem. Mater. 2020, 32, 3922−3929

tested, and no vacancy or atomic mixture was discovered. A typical layered character can be observed for the structure, where the face-shared Mn@$Pt_{12}$ polyhedra layers are intercalated by As layers, as shown in Figure 1a. The distances

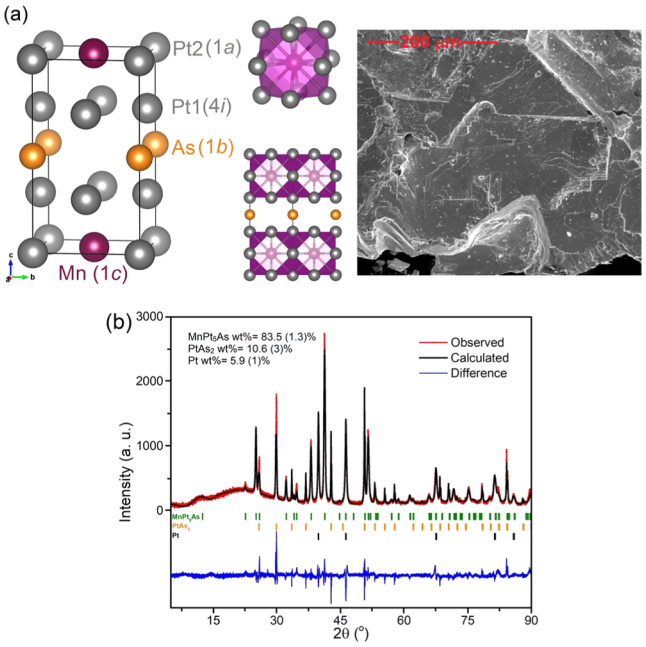


**Figure 1.** (a) Crystal structure of $MnPt_5As$ determined by single-crystal XRD, where purple, gray, and orange balls stand for Mn, Pt, and As atoms, respectively. The crystal picture showing a layered character is on the right. (b) Rietveld fitting of the PXRD pattern from 5 to 90° including contributions from $MnPt_5As$, $PtAs_2$, and Pt phases.

between the two nearest Mn atoms are 3.931 (1) Å within the *ab*-plane and 7.092 (1) Å along the *c*-axis. The lattice parameters of $MnPt_5As$ are 0.5 and 2.9% larger in *a* and *c*, respectively, than those in $MgPt_5As$. The increased lattice parameters in $MnPt_5As$ result in increasing the bond length of Pt1−Pt1 along the *c*-axis from 2.756 Å in $MgPt_5As$ to 3.129 Å in $MnPt_5As$. However, the Mn−Pt distance is ∼2.79 Å, while the Mg−Pt distance is ∼2.84 Å. The shorter atomic Mn−Pt distance indicates that the $Mg^{2+}$ in $MgPt_5As$ can be replaced by the smaller $Mn^{3+}$. Moreover, we have identified a close relationship between the $MnPt_5As$-type structure and unconventional superconductor, $PuCoGa_5$. Pu-centered Ga cuboctahedra (Pu@$Ga_{12}$) and Co-centered Ga cubes (Co@$Ga_8$) in $PuCoGa_5$ can be analogies to Mn@$Pt_{12}$ and As@$Pt_8$ in $MnPt_5As$, respectively.

By fitting the PXRD pattern shown in Figure 1b with the crystal structure obtained from SC-XRD, it can be realized that the majority of the product is $MnPt_5As$(83.5(1) wt %) while there are two nonmagnetic impurity phases identified as $PtAs_2$(10.6(3) and Pt(5.9(1) wt %)). The fitting parameters of the $MnPt_5As$ phase are $X^2$ = 3.62, $R_p$ = 8.99, $R_{wp}$ = 12.0, and $R_{exp}$ = 6.32 and the difference between the observed and calculated patterns is acceptable. No obvious extra phases could be found. We tried to include the fourth phase, MnAs,[53] as possible magnetic impurity but it showed an unreliable result due to the high *R* factor. Regrinding the obtained polycrystalline samples and reannealing were not helpful to make the product purer. Instead, multiple annealing steps lower the degree of crystallization. The observed intensity of the PXRD pattern in such cases was extremely low and most of the minor peaks cannot be identified.

**Magnetic Susceptibility of Polycrystalline $MnPt_5As$.** To investigate the magnetic properties of $MnPt_5As$, polycrystalline samples of $MnPt_5As$ were measured with an external magnetic field of 1000 Oe. The results of both field-cooled (FC) and zero-field-cooled (ZFC) *M* vs *T* are shown in Figure 2. On cooling down the sample, a dramatic increase of

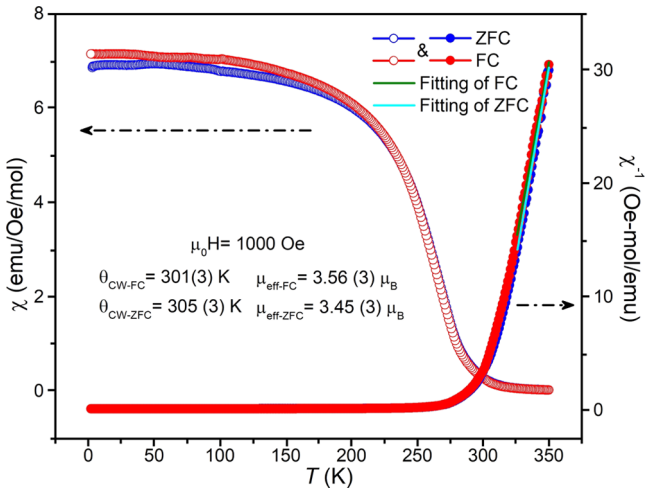


**Figure 2.** Temperature dependence of magnetic susceptibility (empty circles) and inverse magnetic susceptibility (solid circles) of $MnPt_5As$ with ZFC (red) and FC (blue) methods. Green and cyan lines indicate Curie−Weiss fitting lines for FC and ZFC curves, respectively.

magnetic susceptibility is clearly observed near $T_c$ ∼ 300 K, which implies ferromagnetic ordering. An analysis of the inverse susceptibility using the Curie−Weiss (CW) law was modeled using $X = C/(T - \theta_{CW})$, where *X* is the magnetic susceptibility, *C* is the Curie constant, and $\theta_{CW}$ is the Curie−Weiss temperature. The effective moments $\mu_{eff}$ fitted in the high-temperature range (325−345 K) ($\mu_{eff} = \sqrt{8C}\ \mu_B$) are 3.56(3) $\mu_B$ for the FC method and 3.45(3) $\mu_B$ for the ZFC method. The fitted Curie−Weiss temperatures for both methods are 301(3) K (FC) and 305(3) K (ZFC), which is consistent with the ferromagnetic transition. The measurements were conducted on different specimens to confirm the reproducibility.

**Field-Dependent Magnetization in $MnPt_5As$.** The hysteresis loops of magnetization *M*(*H*) measured with applied fields up to 90 kOe at various temperatures from 1.8 to 350 K are shown in Figure 3. The small coercivity (∼15 Oe at 1.8 K) confirms the soft ferromagnetic character of $MnPt_5As$. Figure 3a shows the field dependences of the magnetization per Mn atom. $MnPt_5As$ is magnetized to saturate at $M_s$ ∼ 3.541(1) $\mu_B$/Mn by an external magnetic field of ∼0.7 T at 1.8 K. On increasing the temperature, the saturated moment decreases until 300 K and vanishes at 350 K. In particular, the field dependences of *M*(*H*) at 350 K investigated carefully upon both sweeping up and down of the applied field show paramagnetic properties. The exact saturated moments at different temperatures are determined from the intercepts in Figure 3b by linear fitting each line. The results are consistent with the magnetic susceptibility measurements. The saturated moment observed for $MnPt_5As$ is smaller than what was reported for one of the most well-known Mn-based


https://dx.doi.org/10.1021/acs.chemmater.0c00244
Chem. Mater. 2020, 32, 3922−3929

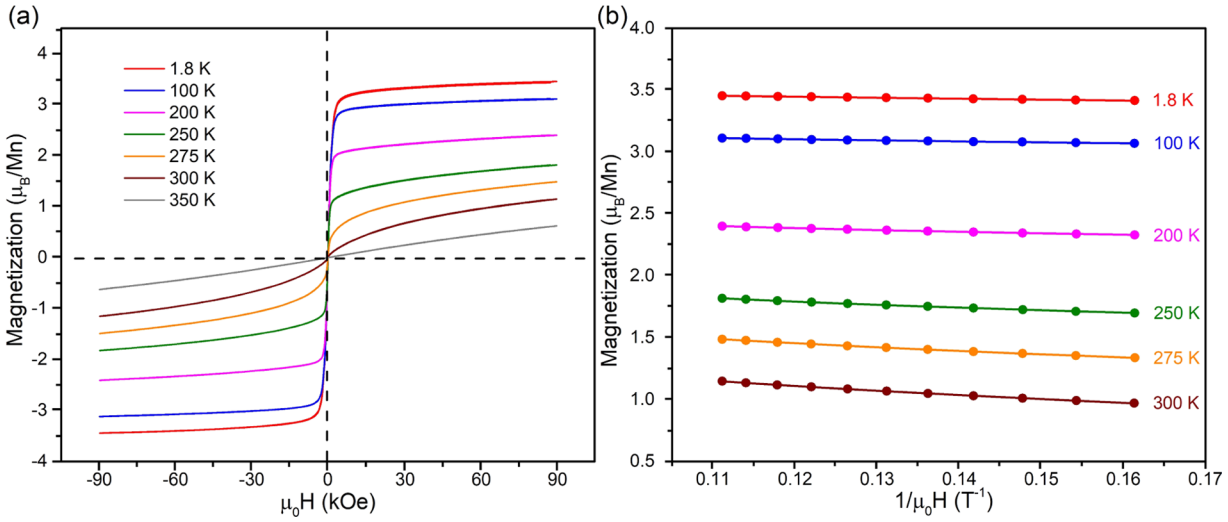


**Figure 3.** (a) Hysteresis loop from −9 to 9 T under various temperatures from 1.8 to 350 K. (b) Magnetization per Mn atom as a function of the inverse magnetic field ($1/\mu_0 H$) where the intercept of each line with linear fitting indicates the saturated magnetic moment under that temperature.

ferromagnets, MnBi, where a saturated moment of ∼4.2 $\mu_B$/Mn can be found.[54] The difference of $M_s$ between MnBi and $MnPt_5As$ might be coming from the larger Mn−Mn distance and weaker Mn−Mn magnetic interactions in $MnPt_5As$ ($d_{Mn-Mn}$ ∼ 3.91 Å in $MnPt_5As$; $d_{Mn-Mn}$ ∼ 3.05 Å in MnBi).

**Resistivity of $MnPt_5As$.** To study the electronic properties of $MnPt_5As$, the resistivity of a small single crystal of $MnPt_5As$ was picked up and measured using the four-probe method. Figure 4 illustrates the temperature dependence of resistivity

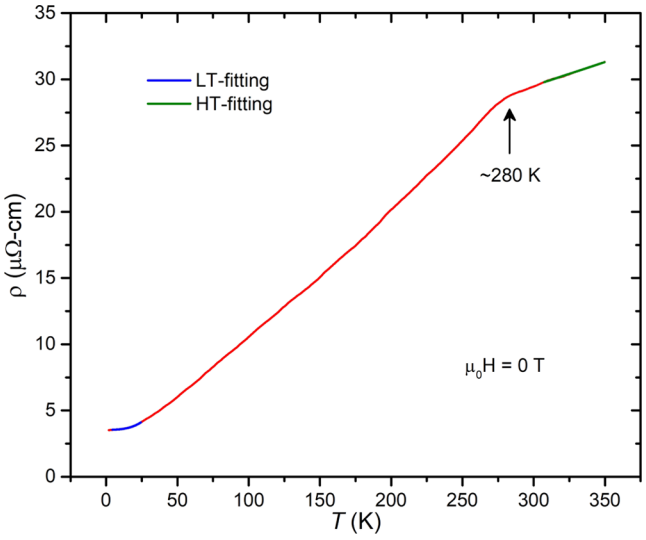


**Figure 4.** Temperature dependence of resistivity for $MnPt_5As$ under 0 T. Green and blue lines stand for the power-law fitting under high- and low-temperature regions.

without an applied magnetic field. The resistivity measurement shows the metallic properties of $MnPt_5As$. An anomaly can be observed around 300 K, which reflects the ferromagnetic ordering transition, similar to other ferromagnetic intermetallics, for example, $Ce_2CoGe_3$, $Ce_5Co_4Ge_{13}$, and $Y(Fe_{1-x}Co_x)_2$.[55,56,55,56] The reason for the kink observed could be that the major contribution of resistivity in $MnPt_5As$ changes from electron−phonon scattering (at a higher temperature) to electron−electron scattering (below the magnetic ordering temperature) while it is possible that additional magnetoresistance contribution develops below $T_c$. A high-quality single crystal may be necessary for further investigation. The resistivity curve was fitted by using a power law $\rho(T) = \rho_0 + AT^n$ where $\rho_0$ is the residual resistivity due to defect scattering, $A$ is a constant, and $n$ is an integer determined by the interaction pattern. At high temperatures (HT) before the magnetic ordering temperature (310−350 K), as shown by the green line, we found a good fit when $n$ equals 1, which means the resistivity has mainly resulted from the collision between electrons and phonons. As the temperature goes down, the phonon contribution decreases significantly, while n is best fitted to be 3 in the low-temperature (LT) region (4−25 K). This confirms that s−d electron scattering is a possible predominant mechanism at low temperatures.[57] The residual resistivity $\rho_0$ for HT and LT regions was fitted to be 18.8(1) and 3.546(3) μΩ cm, respectively. The constant $A$ was fitted to be 0.0356(3) (μΩ cm)/K in the HT range and a much smaller $3.84(6) \times 10^{-5}$ (μΩ cm)/$K^3$ in the LT range.

**Heat Capacity Measurement.** The specific heat of $MnPt_5As$ was measured between 220 and 320 K, as shown in Figure 5. A clear anomaly can be observed starting from ∼300 K with the peak appearing at ∼270 K, which is consistent with the result for the magnetic ordering transition temperature in magnetic susceptibility measurement. The λ-shape anomaly confirms that the magnetic phase transition at room temperature is intrinsic in $MnPt_5As$. Due to the lack of information for the phonon mode and the noisy high-temperature data, we are not able to calculate the magnetic entropy change for $MnPt_5As$.

**Chemical Bonding and the Theoretical Magnetic Structure.** To examine the influence of possible atomic interaction on the structural stability and magnetic properties of $MnPt_5As$, DOS and −COHP by TB-LMTO-ASA calculations were performed. Using the local density approximation (LDA), the DOS curve for $MnPt_5As$ is illustrated in Figure 6a, which emphasizes contributions from the Mn and Pt valence orbitals. Most of the DOS curve below −0.5 eV belong to the Pt 5d band; the Fermi level (−1 to +1 eV) is dominated by a combination of Mn and Pt d orbital contributions, which forms a noticeably sharp and intense peak around 1 eV wide. According to the corresponding −COHP


https://dx.doi.org/10.1021/acs.chemmater.0c00244
Chem. Mater. 2020, 32, 3922−3929

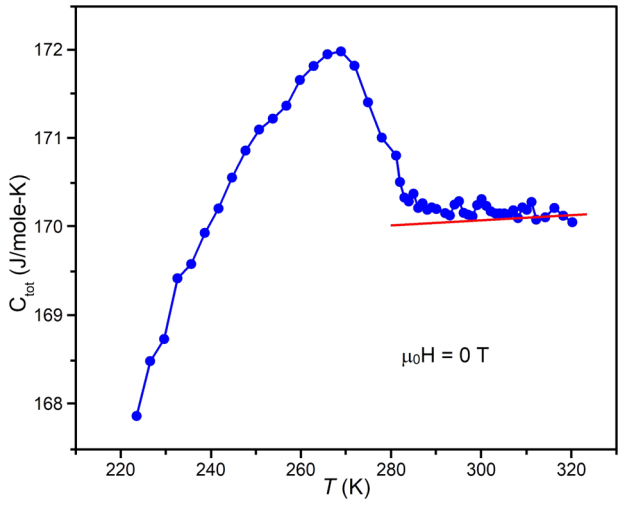


**Figure 5.** Heat capacity measurement conducted between 220 and 320 K with no applied magnetic field. The red line is the proposed baseline.

curves, the wavefunctions contributing to this peak have a strong Pt−Mn and Pt−Pt antibonding character. These features of the LDA−DOS arise from structural influences on the orbital interactions in $MnPt_5As$. In magnetic materials, the tendency of being ferromagnetic ordering can be determined by using the Stoner criterion, which requires a value larger than 1 for the term $N(E_F)I(Mn)$. Evaluation of the Stoner criterion using the Mn partial DOS gives $N(E_F)I(Mn) = 6.3$ where $N(E_F) = 15.5$ $eV^{-1}$ and $I(Mn)$ stands for the exchange−correlation integral, 0.408 eV for Mn.[58] Thus, according to the LDA−DOS curves, $MnPt_5As$ is susceptible to either a structural distortion or ferromagnetism by breaking the spin degeneracy to eliminate the antibonding interactions at the Fermi level.

Applying spin polarization via the local spin density approximation (LSDA), the DOS and −COHP curves for the spin-up and spin-down wavefunctions are illustrated in Figure 6c−e. It is clearly shown that the corresponding Fermi levels shift away from the peaks in the DOS curves and closely approach the pseudogap in both majority and minority spin DOS curves. Moreover, the Pt−Mn and Pt−Pt antibonding states vanish. The integration of the spin-up and spin-down contribution yields a total magnetic moment of 4.55 $\mu_B$ per formula unit for $MnPt_5As$. Interestingly, analysis of the local moments reveals that the magnetic moments arise primarily from the Mn atoms (3.95 $\mu_B$) and slightly from the Pt atoms (0.12 $\mu_B$). The Stoner product in the spin-polarized situation is 2.6, indicating that ferromagnetic ordering is favored. Further investigation will be needed to determine the role of the Pt atoms in the Mn−Mn exchange interaction. Moreover, the majority and minority spin Mn 3d and Pt 5d bands are not fully filled at the Fermi level, which also indicates soft ferromagnetic behavior. The theoretical calculation confirms what is observed experimentally.

**Electronic Structure Calculation.** To estimate the influence of spin−orbit coupling (SOC) on the magnetic properties in $MnPt_5As$, the band structure and density of states (DOS) were also calculated using the WIEN2k program. The electronic structures for $MnPt_5As$ in Figure 7a,b show great consistency with the resistivity measurements, which showed that the compound is metallic. The LDA band structures with/without SOC reveal that the sharp peak in the DOS involves the hybridization of Mn 3d and Pt 5d bands that are relatively flat (nearly dispersionless) near the Brillouin zone boundaries. A saddle point can be observed at the Γ point near the Fermi level ($E_F$) when SOC is not applied, which is broken by SOC when it is included. The SOC effect also opens a gap at some other high-symmetry points. The p orbital of the As atoms and the d orbitals of Mn and Pt atoms are dominant in the energy range we showed, as can be seen in the DOS figures. A van Hove singularity from the d orbitals of the Mn atoms can be observed near $E_F$ when SOC is not considered. However, the SOC effect splits the strong peak in DOS near $E_F$ into two small peaks (indicated by the red arrows). Therefore, the d orbital from the Mn atoms contributes ∼50% less at $E_F$. The Stoner term is calculated to be 8.34 without SOC and 4.41 with considering the SOC effect. The calculated Stoner parameter without SOC from the WIEN2k program is close to the one obtained for the LMTO calculation. Thus, $MnPt_5As$ is theoretically ferromagnetic, consistent with the experimental magnetic measurement.

The three-dimensional Fermi surface demonstrates the distribution of energy bands crossing the Fermi level in the

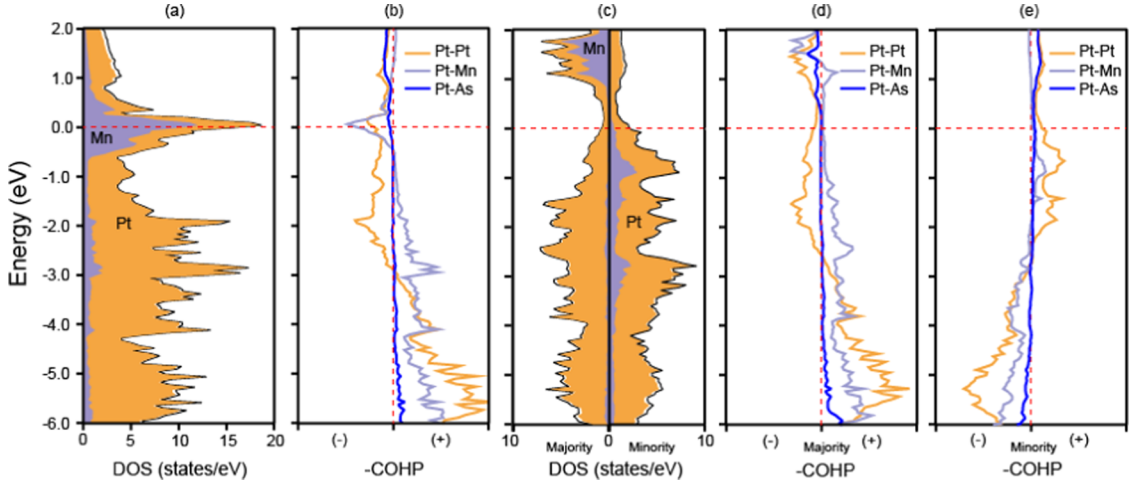


**Figure 6.** (a) Partial DOS curves and (b) −COHP curves of $MnPt_5As$ obtained from nonspin polarization (LDA). (c) Partial DOS curves and (d, e) −COHP curves of $MnPt_5As$ obtained from spin polarization (LSDA).


https://dx.doi.org/10.1021/acs.chemmater.0c00244
Chem. Mater. 2020, 32, 3922−3929

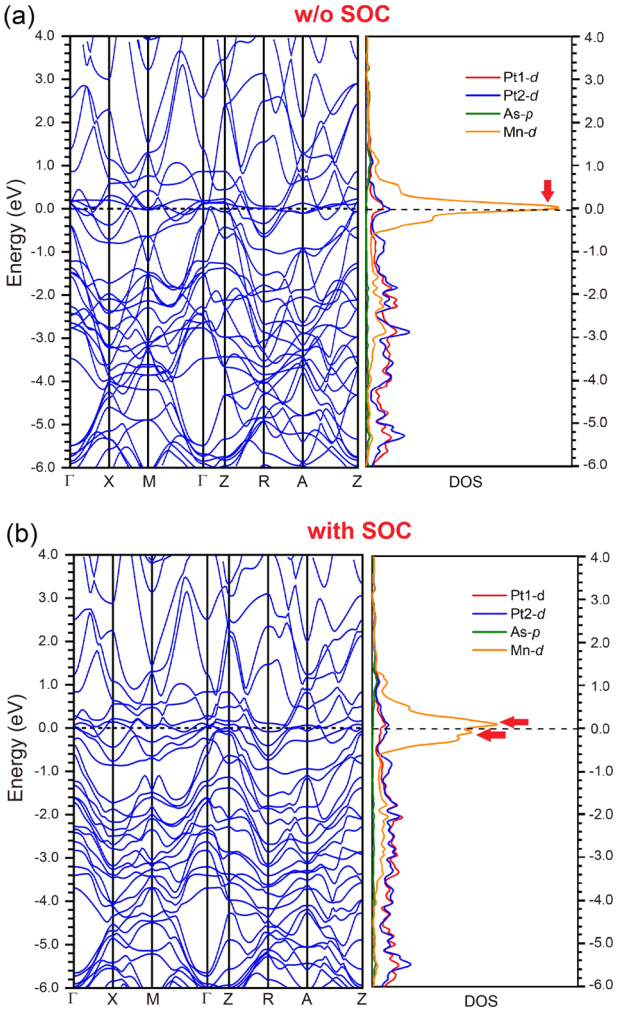


**Figure 7.** Band structure and density of states (DOS) of $MnPt_5As$ (a) without and (b) with consideration of the spin−orbit coupling (SOC) effect. The red arrows indicate the splitting of van Hove singularity on DOS near $E_F$ caused by the SOC effect.

first Brillouin zone (BZ). To estimate the SOC effects on the electronic structure of $MnPt_5As$, the Fermi surfaces with/without SOC were generated and are illustrated in Figure 8. Intuitively, the strong SOC effect on Pt atoms indeed decreases the electronic states within the first BZ, which also is reflected in the density of states. SOC effect mainly influences the Fermi surface at/near the high-symmetry points,

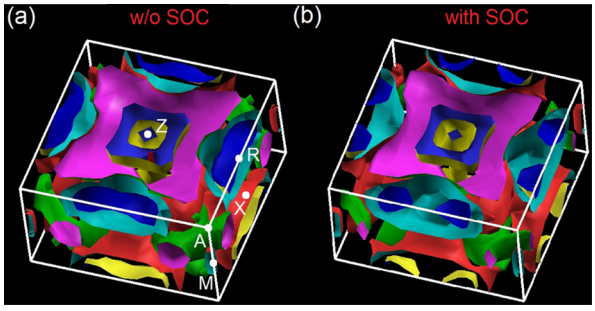


**Figure 8.** Fermi surface of $MnPt_5As$ in the first Brillouin zone of $MnPt_5As$ (a) without and (b) with the spin−orbit coupling effect considered. *Z*, *R*, *A*, *M*, and *X* indicate the position of high-symmetry points. Γ point is at the geometric center of the first BZ.

which are marked in Figure 8 except for the Γ point that is at the geometric center of the first BZ. One can easily tell that by introducing the SOC effect, the saddle point at *R* disappears. The electronic states near the Γ point in the center of the BZ also vanish. Moreover, electronic states near the *A* and *Z* points dramatically reduce after the SOC effect is included.

## CONCLUSIONS

In this paper, we successfully synthesized a new rare-earth-free Pt-rich ferromagnet, $MnPt_5As$. The new material displays a layered tetragonal crystal structure with a space group of *P*4/*mmm*. Magnetic property measurements proved that $MnPt_5As$ is ferromagnetically ordered at room temperature. Resistivity and heat capacity measurements confirm the magnetic property measurements. The theoretical electronic structure demonstrates that Pt−Mn and Pt−Pt antibonding interactions are critical to the ferromagnetic properties in $MnPt_5As$. Moreover, the spin−orbit coupling effect of Pt atoms is essential in decreasing the density of states of the Mn atoms at $E_F$ by splitting the van Hove singularity at the Fermi level, thus lowering the saturated moment. Moreover, $MnPt_5As$ is the first high-$T_c$ magnetic material with this structure-type. It provides a great platform to design and investigate new magnetic materials with targeted functional properties.

## ASSOCIATED CONTENT

### Supporting Information

The Supporting Information is available free of charge at https://pubs.acs.org/doi/10.1021/acs.chemmater.0c00244.

Data of XG_$MnPt_5As$_100919_H_0m (CIF)

## AUTHOR INFORMATION

### Corresponding Author

**Weiwei Xie** − *Department of Chemistry, Louisiana State University, Baton Rouge, Louisiana 70803, United States;* orcid.org/0000-0002-5500-8195; Email: weiweix@lsu.edu

### Author

**Xin Gui** − *Department of Chemistry, Louisiana State University, Baton Rouge, Louisiana 70803, United States*

Complete contact information is available at: https://pubs.acs.org/10.1021/acs.chemmater.0c00244

### Notes

The authors declare no competing financial interest.

## ACKNOWLEDGMENTS

The work at LSU is supported by the Beckman Young Investigator Award and NSF-DMR-1944965.

## REFERENCES

(1) Morón, C.; Cabrera, C.; Morón, A.; García, A.; González, M. Magnetic Sensors Based on Amorphous Ferromagnetic Materials: A Review. *Sensors* **2015**, *15*, 28340−28366.

(2) Parkin, S.; Yang, S.-H. Memory on the Racetrack. *Nat. Nanotechnol.* **2015**, *10*, 195−198.

(3) Averyanov, D. V.; Sadofyev, Y. G.; Tokmachev, A. M.; Primenko, A. E.; Likhachev, I. A.; Storchak, V. G. Direct Epitaxial Integration of the Ferromagnetic Semiconductor EuO with Silicon for Spintronic Applications. *ACS Appl. Mater. Interfaces* **2015**, *7*, 6146−6152.

(4) Mahmoud, W. E.; Al-Ghamdi, A. A.; Al-Agel, F. A.; Al-Arfaj, E.; Shokr, F. S.; Al-Gahtany, S. A.; Alshahrie, A.; Shirbeeny, W.; Bronstein, L. M.; Beall, G. W. Highly Ferromagnetic, Transparent

Conducting Electrode Based on $Ce_{1-x}Cu_xO_2$ Thin Film for Spintronic Applications. *Ceram. Int.* **2015**, *41*, 9101−9106.
(5) Chumak, A. V.; Vasyuchka, V. I.; Serga, A. A.; Hillebrands, B. Magnon Spintronics. *Nat. Phys.* **2015**, *11*, 453−461.
(6) Sengupta, A.; Shim, Y.; Roy, K. Proposal for an All-Spin Artificial Neural Network: Emulating Neural and Synaptic Functionalities Through Domain Wall Motion in Ferromagnets. *IEEE Trans. Biomed. Circuits Syst.* **2016**, *10*, 1152−1160.
(7) Patel, K.; Zhang, J.; Ren, S. Rare-Earth-Free High Energy Product Manganese-Based Magnetic Materials. *Nanoscale* **2018**, *10*, 11701−11718.
(8) Li, D.; Li, Y.; Pan, D.; Zhang, Z.; Choi, C.-J. Prospect and Status of Iron-Based Rare-Earth-Free Permanent Magnetic Materials. *J. Magn. Magn. Mater.* **2019**, *469*, 535−544.
(9) Yüzüak, G. D.; Yüzüak, E.; Elerman, Y. $Hf_2Co_{11}$ Thin Films: Rare-Earth-Free Permanent Nanomagnets. *Thin Solid Films* **2017**, *625*, 115−121.
(10) López-Ortega, A.; Lottini, E.; Fernández, C. D. J.; Sangregorio, C. Exploring the Magnetic Properties of Cobalt-Ferrite Nanoparticles for the Development of a Rare-Earth-Free Permanent Magnet. *Chem. Mater.* **2015**, *27*, 4048−4056.
(11) Kittel, Charles. *Introduction to Solid State Physics*, 8th ed. Wiley: US, 1996.
(12) Mohapatra, J.; Liu, J. P. Rare-Earth-Free Permanent Magnets: The Past and Future. In *Handbook of Magnetic Materials*, Brück, E., Ed.; Elsevier: Oxford, United Kingdom, 2018; Vol. *27*, pp 1−57.
(13) Cui, J.; Kramer, M.; Zhou, L.; Liu, F.; Gabay, A.; Hadjipanayis, G.; Balasubramanian, B.; Sellmyer, D. Current Progress and Future Challenges in Rare-Earth-Free Permanent Magnets. *Acta Mater.* **2018**, *158*, 118−137.
(14) Ibrahim, M.; Masisi, L.; Pillay, P. Design of Variable-Flux Permanent-Magnet Machines Using Alnico Magnets. *IEEE Trans. Ind. Appl.* **2015**, *51*, 4482−4491.
(15) Campbell, R. B.; Julien, C. A. Structure of Alnico V. *J. Appl. Phys.* **1961**, *32*, S192−S194.
(16) Julien, C. A.; Jones, F. G. Alpha-Sub-Gamma Phase in Alnico 8 Alloys. *J. Appl. Phys.* **1965**, *36*, 1173−1174.
(17) Zhou, L.; Miller, M. K.; Lu, P.; Ke, L.; Skomski, R.; Dillon, H.; Xing, Q.; Palasyuk, A.; McCartney, M. R.; Smith, D. J.; et al. Architecture and Magnetism of Alnico. *Acta Mater.* **2014**, *74*, 224−233.
(18) Zhou, L.; Tang, W.; Ke, L.; Guo, W.; Poplawsky, J. D.; Anderson, I. E.; Kramer, M. J. Microstructural and Magnetic Property Evolution with Different Heat-Treatment Conditions in an Alnico Alloy. *Acta Mater.* **2017**, *133*, 73−80.
(19) Patel, K.; Zhang, J.; Ren, S. Rare-Earth-Free High Energy Product Manganese-Based Magnetic Materials. *Nanoscale* **2018**, *10*, 11701−11718.
(20) Kōno, H. On the Ferromagnetic Phase in Manganese-Aluminum System. *J. Phys. Soc. Jpn.* **1958**, *13*, 1444−1451.
(21) Koch, A. J. J.; Hokkeling, P.; vd Steeg, M. G.; De Vos, K. J. New Material for Permanent Magnets on a Base of Mn and Al. *J. Appl. Phys.* **1960**, *31*, S75−S77.
(22) Shukla, A.; Pelton, A. D. Thermodynamic Assessment of the Al-Mn and Mg-Al-Mn Systems. *J. Phase Equilib. Diffus.* **2009**, *30*, 28−39.
(23) Park, J. H.; Hong, Y. K.; Bae, S.; Lee, J. J.; Jalli, J.; Abo, G. S.; Neveu, N.; Kim, S. G.; Choi, C. J.; Lee, J. G. Saturation Magnetization and Crystalline Anisotropy Calculations for MnAl Permanent Magnet. *J. Appl. Phys.* **2010**, *107*, No. 09A731.
(24) Manchanda, P.; Kashyap, A.; Shield, J. E.; Lewis, L. H.; Skomski, R. Magnetic Properties of Fe-Doped MnAl. *J. Magn. Magn. Mater.* **2014**, *365*, 88−92.
(25) Anand, K.; Pulikkotil, J. J.; Auluck, S. Study of Ferromagnetic Instability in $\tau$-MnAl, Using First-Principles. *J. Alloys Compd.* **2014**, *601*, 234−237.
(26) Braun, P. B.; Goedkoop, J. A. An X-Ray and Neutron Diffraction Investigation of the Magnetic Phase Al0.89Mn1.11. *Acta Cryst.* **1963**, *16*, 737−740.
(27) Chen, T.; Stutius, W. The Phase Transformation and Physical Properties of the MnBi and Mn1.08Bi Compounds. *IEEE Trans. Magn.* **1974**, *10*, 581−586.
(28) Cui, J.; Choi, J. P.; Li, G.; Polikarpov, E.; Darsell, J.; Kramer, M. J.; Zarkevich, N. A.; Wang, L. L.; Johnson, D. D.; Marinescu, M.; et al. Development of MnBi Permanent Magnet: Neutron Diffraction of MnBi Powder. *J. Appl. Phys.* **2014**, *115*, No. 17A743.
(29) Yang, Y. B.; Chen, X. G.; Guo, S.; Yan, A. R.; Huang, Q. Z.; Wu, M. M.; Chen, D. F.; Yang, Y. C.; Yang, J. B. Temperature Dependences of Structure and Coercivity for Melt-Spun MnBi Compound. *J. Magn. Magn. Mater.* **2013**, *330*, 106−110.
(30) McGuire, M. A.; Cao, H.; Chakoumakos, B. C.; Sales, B. C. Symmetry-Lowering Lattice Distortion at the Spin Reorientation in MnBi Single Crystals. *Phys. Rev. B* **2014**, *90*, No. 174425.
(31) Zarkevich, N. A.; Wang, L.-L.; Johnson, D. D. Anomalous Magneto-Structural Behavior of MnBi Explained: A Path Towards an Improved Permanent Magnet. *APL Mater.* **2014**, *2*, No. 032103.
(32) Cui, J.; Choi, J.-P.; Polikarpov, E.; Bowden, M. E.; Xie, W.; Li, G.; Nie, Z.; Zarkevich, N.; Kramer, M. J.; Johnson, D. Effect of Composition and Heat Treatment on MnBi Magnetic Materials. *Acta Mater.* **2014**, *79*, 374−381.
(33) Brabers, J. H. V. J.; Buschow, K. H. J.; de Boer, F. R. Field-Induced First-Order Antiferromagnetic-Ferromagnetic Transitions in $RMn_2Ge_2$ Compounds and Their Relation to the Magnetostriction of the Mn Sublattice. *Phys. Rev. B* **1999**, *59*, 9314.
(34) Brabers, J. H. V. J.; Duijn, V. H. M.; De Boer, F. R.; Buschow, K. H. J. Magnetic Properties of Rare-Earth Manganese Compounds of the $RMn_6Ge_6$ Type. *J. Alloy Compd.* **1993**, *198*, 127−132.
(35) Brabers, J. H. V. J.; Nolten, A. J.; Kayzel, F.; Lenczowski, S. H. J.; Buschow, K. H. J.; de Boer, F. R. Strong Mn-Mn Distance Dependence of the Mn Interlayer Coupling in $SmMn_2Ge_2$-Related Compounds and Its Role in Magnetic Phase Transitions. *Phys. Rev. B* **1994**, *50*, 16410.
(36) Beleanu, A.; Kiss, J.; Kreiner, G.; Köhler, C.; Müchler, L.; Schnelle, W.; Burkhardt, U.; Chadov, S.; Medvediev, S.; Ebke, D.; et al. Large Resistivity Change and Phase Transition in the Antiferromagnetic Semiconductors LiMnAs and LaOMnAs. *Phys. Rev. B* **2013**, *88*, No. 184429.
(37) Petrovic, C.; Pagliuso, P. G.; Hundley, M. F.; Movshovich, R.; Sarrao, J. L.; Thompson, J. D.; Fisk, Z.; Monthoux, P. Heavy-Fermion Superconductivity in $CeCoIn_5$ at 2.3 K. *J. Phys.: Condens. Matter* **2001**, *13*, L337.
(38) Schulz, S.; Nechaev, I. A.; Güttler, M.; Poelchen, G.; Generalov, A.; Danzenbächer, S.; Chikina, A.; Seiro, S.; Kliemt, K.; Vyazovskaya, A. Y.; Kim, T. K.; et al. Emerging 2D-Ferromagnetism and Strong Spin-Orbit Coupling at the Surface of Valence-Fluctuating EuIr2Si2. *npj Quantum Mater.* **2019**, *4*, No. 26.
(39) Khan, S. A.; Blaha, P.; Ebert, H.; Minár, J.; Šipr, O. Magnetocrystalline Anisotropy of FePt: A Detailed View. *Phys. Rev. B* **2016**, *94*, No. 144436.
(40) Kabir, A.; Hu, J.; Turkowski, V.; Wu, R.; Camley, R.; Rahman, T. S. Effect of Structure on the Magnetic Anisotropy of $L1_0$ FePt Nanoparticles. *Phys. Rev. B* **2015**, *92*, No. 054424.
(41) Pfisterer, M.; Nagorsen, G. Zur Struktur Ternärer Übergangs-metallarsenide/On the Structure of Ternary Arsenides. *Z. Naturforsch. B* **2014**, *35*, 703−704.
(42) Jesus, S.; Borges, O. Recent Developments in the Nasal Immunization against Anthrax. *World J. Vaccines* **2011**, *01*, 79−91.
(43) Sheldrick, G. M. Crystal Structure Refinement with SHELXL. *Acta Crystallogr., Sect. C: Struct. Chem.* **2015**, *71*, 3−8.
(44) *SMART*. Bruker AXS Inc.: Madison, WI, USA, 2012. https://www.bruker.com/products/x-ray-diffraction-and-elemental-analysis/single-crystal-x-ray-diffraction/sc-xrd-software/overview/sc-xrd-software/apex3.html. (date of access: April 10, 2020).
(45) Walker, N.; Stuart, D. An Empirical Method for Correcting Diffractometer Data for Absorption Effects. *Acta Crystallogr., Sect. A: Found. Crystallogr.* **1983**, *39*, 158−166.
(46) Elstner, M.; Porezag, D.; Jungnickel, G.; Elsner, J.; Haugk, M.; Frauenheim, Th.; Suhai, S.; Seifert, G. Self-Consistent-Charge

Density-Functional Tight-Binding Method for Simulations of Complex Materials Properties. *Phys. Rev. B* **1998**, *58*, 7260−7268.
(47) Andersen, O. K.; Jepsen, O. Explicit, First-Principles Tight-Binding Theory. *Phys. Rev. Lett.* **1984**, *53*, 2571−2574.
(48) Krier, G.; Jepsen, O.; Burkhardt, A.; Andersen, O. K. *The TB-LMTO-ASA Program*; Stuttgart, April, 1995.
(49) Blaha, P.; Schwarz, K.; Sorantin, P.; Trickey, S. B. Full-Potential, Linearized Augmented Plane Wave Programs for Crystalline Systems. *Comput. Phys. Commun.* **1990**, *59*, 399−415.
(50) Wimmer, E.; Krakauer, H.; Weinert, M.; Freeman, A. J. Full-Potential Self-Consistent Linearized-Augmented-Plane-Wave Method for Calculating the Electronic Structure of Molecules and Surfaces: $O_2$ Molecule. *Phys. Rev. B* **1981**, *24*, 864−875.
(51) Perdew, J. P.; Wang, Y. Accurate and Simple Analytic Representation of the Electron-Gas Correlation Energy. *Phys. Rev. B* **1992**, *45*, 13244−13249.
(52) King-Smith, R. D.; Vanderbilt, D. Theory of Polarization of Crystalline Solids. *Phys. Rev. B* **1993**, *47*, 1651−1654.
(53) Zieba, A.; Selte, K.; Kjekshus, A.; Andresen, A. F.; et al. Phase Transitions in MnAs. *Acta Chem. Scand.* **1978**, *32*, 173−177.
(54) Yang, J. B.; Yang, Y. B.; Chen, X. G.; Ma, X. B.; Han, J. Z.; Yang, Y. C.; Guo, S.; Yan, A. R.; Huang, Q. Z.; Wu, M. M.; Chen, D. F. Anisotropic Nanocrystalline MnBi with High Coercivity at High Temperature. *Appl. Phys. Lett.* **2011**, *99*, No. 082505.
(55) Soudé, A.; Pikul, A. P.; Wiśniewski, P.; Tougait, O.; Pasturel, M.; Kaczorowski, D.; Noël, H. Magnetic, Electric and Thermoelectric Properties of Ternary Intermetallics from the Ce−Co−Ge System. *Intermetallics* **2011**, *19*, 1201−1206.
(56) Guzdek, P.; Pszczoła, J.; Chmist, J.; Stoch, P.; Stoch, A.; Suwalski, J. Electrical Resistivity and Mössbauer Effect Studies of $Y(Fe_{1-x}Co_x)_2$ Intermetallics. *J. Alloy. Compd.* *520*, 72 76. DOI: 10.1016/j.jallcom.2011.12.081.
(57) Meaden, G. T. *Electrical Resistance of Metals*; The International Cryogenics Monograph Series: Springer US, 1965.
(58) Janak, J. F. Uniform Susceptibilities of Metallic Elements. *Phys. Rev. B* **1977**, *16*, 255−262.


https://dx.doi.org/10.1021/acs.chemmater.0c00244
*Chem. Mater.* 2020, 32, 3922−3929